



HAL
open science

Hybrid regularized Lattice-Boltzmann modelling of premixed and non-premixed combustion processes

M. Tayyab, S. Zhao, Y. Feng, Pierre Boivin

► To cite this version:

M. Tayyab, S. Zhao, Y. Feng, Pierre Boivin. Hybrid regularized Lattice-Boltzmann modelling of premixed and non-premixed combustion processes. *Combustion and Flame*, 2020, 211, pp.173-184. <10.1016/j.combustflame.2019.09.029>. <hal-02346556>

HAL Id: hal-02346556

<https://hal.science/hal-02346556v1>

Submitted on 5 Nov 2019

HAL is a multi-disciplinary open access archive for the deposit and dissemination of scientific research documents, whether they are published or not. The documents may come from teaching and research institutions in France or abroad, or from public or private research centers.

L'archive ouverte pluridisciplinaire HAL, est destinée au dépôt et à la diffusion de documents scientifiques de niveau recherche, publiés ou non, émanant des établissements d'enseignement et de recherche français ou étrangers, des laboratoires publics ou privés.



HAL Authorization

Hybrid regularized Lattice-Boltzmann modelling of premixed and non-premixed combustion processes.

M. Tayyab^a, S. Zhao^a, Y. Feng^a, P. Boivin^{1a}

^a*Aix Marseille Univ, CNRS, Centrale Marseille, M2P2, Marseille, France*

Abstract

A Lattice-Boltzmann model for low-Mach reactive flows is presented, built upon our recently published model (Comb & Flame, 196, 2018). The approach is hybrid and couples a Lattice-Boltzmann solver for the resolution of mass and momentum conservation and a finite difference solver for the energy and species conservation. Having lifted the constant thermodynamic and transport properties assumptions, the model presented now fully accounts for the classical reactive flow thermodynamic closure: each component is assigned NASA coefficients for calculating its thermodynamic properties. A temperature-dependent viscosity is considered, from which are deduced thermo-diffusive properties via specification of Prandtl and component-specific Schmidt numbers. Another major improvement from our previous contribution is the derivation of an advanced collision kernel compatible of multi-component reactive flows stable in high shear flows. Validation is carried out first on premixed configurations, through simulation of the planar freely propagating flame, the growth of the associated Darrieus-Landau instability and three regimes of flame-vortex interaction. A double shear layer test case

¹Corresponding author: pierre.boivin@univ-amu.fr

including a flow-stabilized diffusion flame is then presented and results are compared with DNS simulations, showing excellent agreement.

Keywords: lattice Boltzmann; reacting flows; combustion; detailed kinetics

1. Introduction

Motivated by the rapid development of Lattice-Boltzmann (LB) methods in the field of low-Mach external aerodynamics and aeroacoustics [1], and particularly its potential as an engineering tool [2–7] we recently proposed a hybrid LB framework able to tackle combustion in low-Mach flows [8] in line with the quest of extending the LB capabilities to reactive flows [9–15].

Based on nearest neighbor lattices, the model previously proposed in [8] is easy to implement, but was derived under constant heat capacity and single-step chemistry assumptions, a stark limitation compared to state-of-the-art combustion softwares. A second limitation resides in the simple collision model, merely derived from the BGK model, known to have serious limitations in complex flows [16–22].

This contribution aims at lifting these two limitations as to make the model fully functional for the simulation of reactive flows, including detailed chemistry description.

Lifting the first limitation is attained through integration of the classical thermodynamic closure based on NASA polynomial coefficients [23], as used in CHEMKIN [24], or CANTERA [25]. Detailed chemistry is also accounted for, through a 12-step mechanism for H₂-air combustion [26] derived from the San Diego mechanism [27]. Each of the nine species is assigned a Schmidt number relating its diffusion properties with a temperature-dependent viscosity

coefficient, and thermal diffusion is defined via a constant Prandtl number as in [28].

The second limitation is equally lifted, after derivation of a new collision model compatible with thermal, multicomponent flows. This was achieved following Jacob et al [29], who recently proposed a robust collision model in the context of single-component athermal LBM showing promising results for a wide range of applications [30–34]. As further discussed in this study, the collision kernel adopts a regularization strategy [35] in which the non-hydrodynamic moments of the distribution function (or ghost modes) relax infinitely fast to equilibrium. This strategy is similar to the popular Multiple Relaxation Time (MRT) models [36–39], in which these modes relax at a finite rate.

Validation is carried out by comparisons with CANTERA computations [25] for the planar premixed flame propagation. To further demonstrate the capability of the model in premixed configurations, the Darrieus-Landau instability is simulated, and the associated growth-rate is compared with asymptotic descriptions [40–42], showing good agreement for the linear onset of the instability. To conclude the validation regarding premixed combustion, vortex-flame interactions are simulated, allowing to recover three regimes classically observed experimentally and numerically [43–47].

Next, the capabilities of the model are presented through comparison with Direct Numerical Simulations (DNS) on a double periodic shear-layer including auto-ignition and establishment of a diffusion flame in between the streams. That test case – besides being highly challenging numerically – highlights the accuracy of the proposed model at a reasonable CPU cost.

The paper is organized as follows. First, the LB combustion model is presented, with extensive implementation details. The model is then validated, in premixed and non-premixed combustion test cases. Following the validation, cost and stability issues are discussed prior to drawing conclusions.

2. Governing equations: continuous formulation

2.1. Mass and momentum conservation: Lattice Boltzmann approach

The Boltzmann equation models the gas kinetics with the particle velocity distribution function (VDF) $f(\mathbf{x}, \boldsymbol{\xi}, t)$, which presents the probability density of finding (virtual) gas particles at position \mathbf{x} with velocity $\boldsymbol{\xi}$ at time t . Using the single-relaxation-time collision model of Bhatnagar-Gross-Krook (BGK) [48], the evolution of VDF through phase space and time can be written as

$$\frac{\partial f}{\partial t} + \xi_\alpha \frac{\partial f}{\partial x_\alpha} = -\frac{1}{\tau} (f - f^{\text{eq}}) , \quad (1)$$

where τ is the relaxation time associated to the dynamic viscosity of the fluid and f^{eq} is the Maxwell-Boltzmann equilibrium distribution function associated to the local thermodynamic state

$$f^{\text{eq}} = \frac{\rho}{(2\pi\bar{\tau}T)^{D/2}} \exp\left(-\frac{|\boldsymbol{\xi} - \mathbf{u}|^2}{2\bar{\tau}T}\right) , \quad (2)$$

with ρ and \mathbf{u} being respectively the mixture mass volume and velocity, D the spatial dimension, T the temperature and $\bar{\tau}$ the gas constant of the mixture

$$\bar{\tau} = R/\overline{W} . \quad (3)$$

$R = 8.3145$ J/mol/K is the universal gas constant and \overline{W} is the molecular weight. In principle, (2) is valid for mono-constituent gas, for which the

molecular weight is constant. Here, however, we'll consider an identical equilibrium distribution function for multi-component gas mixtures introducing the mean molecular weight

$$\bar{W} = \frac{1}{\sum_k Y_k/W_k}, \quad (4)$$

where Y_k is the k -th component mass fraction and W_k its molecular weight. It will be shown further that the multi-component macroscopic conservation equations are nonetheless recovered.

Under this formalism, the macroscopic variables ρ and \mathbf{u} are obtained from the VDF through

$$\begin{aligned} \rho &= \int f d\boldsymbol{\xi}, \\ \rho \mathbf{u} &= \int f \boldsymbol{\xi} d\boldsymbol{\xi}. \end{aligned} \quad (5)$$

The Chapman-Enskog (CE) expansion [1] in the low-Mach number limit leads to the following macroscopic mass and momentum equations

$$\begin{aligned} \frac{\partial \rho}{\partial t} + \frac{\partial}{\partial x_\alpha} (\rho u_\alpha) &= 0, \\ \frac{\partial \rho u_\alpha}{\partial t} + \frac{\partial}{\partial x_\beta} (\rho u_\alpha u_\beta) &= -\frac{\partial p}{\partial x_\alpha} + \frac{\partial \mathcal{T}_{\alpha\beta}}{\partial x_\beta}, \end{aligned} \quad (6)$$

where

$$p = \rho \bar{r} T \quad (7)$$

is the classical ideal gas thermodynamic closure, and $\mathcal{T}_{\alpha\beta}$ is the viscous stress tensor

$$\mathcal{T}_{\alpha\beta} = 2\mu S_{\alpha\beta} = \mu \left[\frac{\partial u_\beta}{\partial x_\alpha} + \frac{\partial u_\alpha}{\partial x_\beta} \right], \quad (8)$$

with μ the dynamic viscosity. Note that the bulk viscosity is neglected, as often in the combustion community [49, 50].

The CE expansion, provided in AppendixA, differs from the classical one [1] in that the perfect gas equation of state is recovered instead of the athermal EOS. It also differs from our recent study [31] as (i) the gas is multi-component, e.g. \bar{r} in (3) is not a constant and (ii) additional equations for gas components and energy are required to close the system, to account for non-unity Prandtl and Lewis numbers, as well as source terms between the gas components. AppendixA should be read along with Section 3, as it provides most technical details as well as a detailed discussion.

2.2. Energy and species conservation

Mass conservation of species k is considered following

$$\rho \frac{\partial Y_k}{\partial t} + \rho u_\alpha \frac{\partial Y_k}{\partial x_\alpha} = \frac{\partial}{\partial x_\alpha} (-\rho V_{k,\alpha}) + \dot{\omega}_k, \quad (9)$$

where $\dot{\omega}_k$ is the net chemical production rate of species k , and $V_{k,\alpha}$ is its diffusion velocity [49].

The energy conservation is considered by the balance equation of the enthalpy. Following the multi-component ideal gas thermodynamic closure, the enthalpy of a gas mixture consisting of N species is defined as

$$h = \sum_{k=1}^N h_k Y_k, \quad h_k = \int_{T_0}^T C_{p,k}(T) dT + \Delta h_{f,k}^0, \quad (10)$$

where $C_{p,k}(T)$ is the constant pressure heat capacity of species k at temperature T , and $\Delta h_{f,k}^0$ its formation enthalpy [49]. The conservation law of enthalpy reads

$$\rho \frac{\partial h}{\partial t} + \rho u_\alpha \frac{\partial h}{\partial x_\alpha} = \frac{Dp}{Dt} - \frac{\partial q_\alpha}{\partial x_\alpha} + \mathcal{T}_{\alpha\beta} \frac{\partial u_\alpha}{\partial x_\beta}. \quad (11)$$

where $\frac{Dp}{Dt} = \frac{\partial p}{\partial t} + u_\alpha \frac{\partial p}{\partial x_\alpha}$ is the substantial derivative of pressure, usually neglected in low-Mach combustion applications. The heat flux q_α reads

$$q_\alpha = -\lambda \frac{\partial T}{\partial x_\alpha} + \rho \sum_{k=1}^N h_k Y_k V_{k,\alpha}, \quad (12)$$

with λ the thermal conductivity.

3. Model implementation

3.1. Discretization on standard lattices

Following classical LB models, the particle velocity $\boldsymbol{\xi}$ in Eq. (1) is discretized as a finite dimension velocity space. Our choice lies with nearest neighbors lattices (D2Q9, D3Q19) for their low associated cost. Such discretization strategy being found throughout the LBM literature (e.g. [51]), let us simply indicate that the choice of lattice $DnQm$ set defines, besides the discrete velocities \mathbf{c}_i ($i = 1, \dots, m$), the lattice sound speed c_s and w_i , the Gaussian weights associated to each discrete velocity \mathbf{c}_i .

With these definitions,

$$f_i(\mathbf{x}, t) = \frac{w_i}{\omega(\mathbf{c}_i)} f(\mathbf{x}, \mathbf{c}_i, t), \quad (13)$$

and Eq. (1) can be written at the accuracy of the quadrature as

$$\frac{\partial f_i}{\partial t} + c_{i\alpha} \frac{\partial f_i}{\partial x_\alpha} = -\frac{1}{\tau} (f_i - f_i^{\text{eq}}). \quad (14)$$

This equation is further discretized in space and time with second-order accuracy [51] as

$$\bar{f}_i(x_\alpha + c_{i\alpha} \delta t, t + \delta t) = \bar{f}_i(x_\alpha, t) - \frac{\delta t}{\tau} [\bar{f}_i(x_\alpha, t) - f_i^{\text{eq}}(x_\alpha, t)], \quad (15)$$

where the time step δt is classically linked to the spatial discretization through definition of the set of lattices *DnQm* [1]. Note that introduction of \bar{f}_i and $\bar{\tau}$ in (15) as

$$\bar{f}_i = f_i - \frac{\delta t}{2} \Omega_i = f_i - \frac{\delta t}{2} \left[-\frac{1}{\tau} (f_i - f_i^{\text{eq}}) \right], \quad (16)$$

and

$$\bar{\tau} = \tau + \frac{\delta t}{2}, \quad (17)$$

is a necessary change of variable to ensure the second-order accuracy in time [51]. In practice, all physical quantities are normalized in the LBM code using the grid size δx for length, the time step δt for time and a reference density ρ_0 (combined with δx) for mass.

3.2. Hybrid regularized collision model

Single relaxation time models often lead to numerical instabilities in shear-flows [52], and are unable to tackle the test case of Fig. 5. To increase numerical stability in such flows, a possibility is to include multiple relaxation times models (see, e.g. [36–39]), in which relaxation times for the higher-order moments (neither corresponding to the mass conservation nor the momentum) are carefully tuned to optimize the stability properties. On the same idea, it was later proposed [17] to simply suppress the non-equilibrium part of these modes, in so-called *regularized* collision kernels. Here a regularization step is adapted from [16, 18, 29] to the multi-component flow model. The regularization strategy reconstructs \bar{f}_i before collision by considering

$$\bar{f}_i = f_i^{\text{eq}} + \bar{f}_i^{\text{neq}}, \quad (18)$$

with both the equilibrium (f_i^{eq}) and off-equilibrium part (\bar{f}_i^{neq}) of the VDF confined in the Hermite basis. Following [8, 18, 29], the equilibrium VDF are

truncated up to third order to reduce the non-Galilean defect

$$f_i^{\text{eq}} = w_i \left[a^{(0),\text{eq}} + \frac{a_\alpha^{(1),\text{eq}}}{c_s^2} \mathcal{H}_\alpha^{(1)}(\mathbf{c}_i) + \frac{a_{\alpha\beta}^{(2),\text{eq}}}{2c_s^4} \mathcal{H}_{\alpha\beta}^{(2)}(\mathbf{c}_i) + \frac{a_{\alpha\beta\gamma}^{(3),\text{eq}}}{6c_s^6} \mathcal{H}_{\alpha\beta\gamma}^{(3)}(\mathbf{c}_i) \right], \quad (19)$$

with the Hermite polynomial tensors associated to each discrete velocity \mathbf{c}_i defined as

$$\begin{aligned} \mathcal{H}_\alpha^{(1)}(\mathbf{c}_i) &= c_{i\alpha}, \\ \mathcal{H}_{\alpha\beta}^{(2)}(\mathbf{c}_i) &= c_{i\alpha}c_{i\beta} - \delta_{\alpha\beta}c_s^2, \\ \mathcal{H}_{\alpha\beta\gamma}^{(3)}(\mathbf{c}_i) &= c_{i\alpha}c_{i\beta}c_{i\gamma} - c_s^2(\mathbf{c}_i\boldsymbol{\delta})_{\alpha\beta\gamma}, \end{aligned} \quad (20)$$

and the associated equilibrium coefficients $a^{(i),\text{eq}}$ reading

$$a^{(0),\text{eq}} = \rho, \quad (21a)$$

$$a_\alpha^{(1),\text{eq}} = \rho u_\alpha, \quad (21b)$$

$$a_{\alpha\beta}^{(2),\text{eq}} = \rho [u_\alpha u_\beta + c_s^2 (\theta - 1) \delta_{\alpha\beta}], \quad (21c)$$

$$a_{\alpha\beta\gamma}^{(3),\text{eq}} = \rho [u_\alpha u_\beta u_\gamma + c_s^2 (\theta - 1) (\mathbf{u}\boldsymbol{\delta})_{\alpha\beta\gamma}], \quad (21d)$$

where θ is the normalized temperature, defined as in our initial model [8]

$$\theta = \frac{\bar{r}T}{c_s^2}, \quad (22)$$

and the tensor $\mathbf{u}\boldsymbol{\delta}$ reads

$$(\mathbf{u}\boldsymbol{\delta})_{\alpha\beta\gamma} = \delta_{\alpha\beta}u_\gamma + \delta_{\gamma\beta}u_\alpha + \delta_{\alpha\gamma}u_\beta. \quad (23)$$

Note that, consistently with the Hermite space, the lattice sound speed is linked to the space-time discretization as $c_s \equiv \delta x / \delta t / \sqrt{3}$ [53].

The non-equilibrium part of VDF are truncated up to second order to recover a correct viscous tensor [29]

$$\bar{f}_i^{\text{neq}} = \frac{w_i \bar{a}_{\alpha\beta}^{(2),\text{neq}}}{2c_s^4} \mathcal{H}_{\alpha\beta}^{(2)}(\mathbf{c}_i). \quad (24)$$

In the present regularized collision model, the off-equilibrium coefficients $\bar{a}_{\alpha\beta}^{(2),\text{neq}}$ are evaluated through two different approximations, hence its given name: *hybrid regularized collision model* [29].

The first approximation arises from direct projection of \bar{f}_i^{neq} as

$$\bar{a}_{\alpha\beta}^{(2),\text{neq,PR}} = \sum_{i=1}^m \left[(\bar{f}_i - f_i^{\text{eq}}) \mathcal{H}_{\alpha\beta}^{(2)}(\mathbf{c}_i) \right] \quad (25)$$

while the second approximation is computed as to best approximate the viscous tensor $S_{\alpha\beta}$ in Eq. (8). That term is assessed via finite difference method (hence the FD subscript)

$$\bar{a}_{\alpha\beta}^{(2),\text{neq,FD}} = -2p\bar{\tau}S_{\alpha\beta}^{\text{FD}}. \quad (26)$$

As shown by Jacob et al. [29] and further demonstrated in this article, excellent numerical stability of the collision model is obtained through combination of (25) and (26) as

$$\bar{a}_{\alpha\beta}^{(2),\text{neq}} = \sigma \bar{a}_{\alpha\beta}^{(2),\text{neq,PR}} + (1 - \sigma) \bar{a}_{\alpha\beta}^{(2),\text{neq,FD}} \quad (27)$$

where $\sigma \in [0, 1]$ is a free parameter.

3.3. Correction term and final model

Last, let us introduce an additional forcing term to be included in the LBM equation (15). That correction corresponds to the deviation due to defect of symmetry of lattices (D2Q9, D3Q19, D3Q27) on the third order moment [8, 54], and reads

$$s_i = \frac{w_i}{2c_s^4} \mathcal{H}_{\alpha\alpha}^{(2)}(\mathbf{c}_i) \partial_\alpha \left[\rho u_\alpha (3c_s^2 - 3c_s^2\theta - u_\alpha^2) \right], \quad (28)$$

affecting the LB equation (15) as

$$\bar{f}_i(x_\alpha + c_{i\alpha}\delta t, t + \delta t) = f_i^{\text{eq}}(x_\alpha, t) + \left(1 - \frac{\delta t}{\tau}\right) \bar{f}_i^{\text{neq}} + \frac{\delta t}{2} s_i. \quad (29)$$

The correction term's first two moments being mass and momentum preserving, the reconstruction of the macroscopic variables from the distribution functions remain unaffected:

$$\rho = \sum_{i=1}^m \bar{f}_i, \quad \rho u_\alpha = \sum_{i=1}^m c_{i\alpha} \bar{f}_i. \quad (30)$$

Note that, as shown in [31], additional correction terms are necessary for high-Mach flows with the D3Q19 stencil. They are neglected here as the Mach numbers encountered remain moderate.

3.4. FD solver specifics

In parallel of the LB solver, we use a FD solver to solve the species (9) and energy (11) conservation equations. The flowchart of the code is identical to that presented in our initial model [8]. Through systematic testing of the different finite differences methods, we retained the method presented in this Section.

The advection-diffusion part of (9) and (11) (e.g. without source term) is solved using the following strategy, arguably the simplest and most robust one could think of:

1. The LB and FD solver use the same time-step, and first order forward Euler integration is used. It is important to note that strong-stability-preserving Runge-Kutta (SSPRK) methods [55] up to fourth order have been implemented, with no apparent effect on the validations carried out.

2. Second order central difference operators are used for convection and diffusion. Note that introducing 10% of first-order up-winding on the convective operator was found to enhance numerical stability in high shear flows (as in Section 5)

The chemical source term is applied through a Strang-method splitting [56, 57], allowing the use of sub time-steps for the chemical integration when necessary (as for an implicit chemical solver). Similarly, the diffusion term may be easily split from the advection step, should it become necessary.

3.5. Boundary conditions

This model being new, future work is required to present implementation of complex boundary conditions. Following our initial strategy [8], we picked validation test cases requiring rather simple boundary conditions. Besides the trivial periodic boundary condition of the double shear layer test case, only basic velocity inlet and zero-gradient outlet boundary conditions were necessary for this work.

A non-equilibrium bounce back scheme with a regularization procedure [17] is employed at the inlets for the LB solver, allowing to set all velocity components and the pressure (or density). (h, Y_k) are hard-coded at inlets for the FD solver accordingly with the target temperature and composition.

Outlets are treated as zero-gradient boundaries on microscopic distribution functions f_i as well as h and Y_k variables.

4. Premixed combustion validation test cases

Let us now present validations and discussions of the hybrid model presented above. To that aim, the model was implemented in the PROLB solver

[18, 29, 54, 58] considering the following aspects:

Thermodynamic closure is ensured via the classical NASA polynomial formulation for each gaseous constituent [23], as in CHEMKIN [24].

Viscosity is set via a temperature power-law (B.2).

Transport of heat and species are defined via constant Prandtl (B.1) and individual Schmidt numbers (B.4), as done for instance in the AVBP solver [28].

Chemistry for hydrogen-air is accounted for via a 12-step skeletal mechanism [26] involving nine species (see Tab. B.4).

Details about these four points are gathered in AppendixB. Since they were not necessary in the development of Sections 2 and 3, they may be easily changed in future works.

The solver being based on the D3Q19 lattice, 1D results presented below use periodic conditions along the y and z axis (with a single cell in either direction), and 2D results use periodic conditions along the z axis. 3D results will be presented in future publications.

4.1. 1D premixed flame

Let us now consider the standard freely propagating flame configuration, following the setup of [8].

The computational domain is pseudo one-dimensional of length $L = 10$ mm, with grid size of 10^{-5} m. At the left of the domain, the velocity is set to an arbitrary value U_f , and the right boundary is left open (zero gradient).

Periodic boundary conditions are applied to the other boundaries (corresponding to the y and z directions). The time step is $\delta_t = 7.21 \times 10^{-9}$ s.

Initial conditions consist of two half-domains initially at $u = U_f$, and a sharp transition at $L/2$, separating the fresh and burnt gases. The left side of the domain corresponds to the fresh gases, whereas the right side corresponds to the burnt gases initialized at the corresponding CANTERA-computed thermo-chemical equilibrium – provided in Table B.5 of AppendixB.

As in our previous contribution [8], we measure the flame speed as

$$S_L = \lim_{t \rightarrow \infty} \left(U_f - \frac{\rho_f U_f - \rho_b U_b}{\rho_f - \rho_b} \right), \quad (31)$$

where the subscript f represents fresh and b burnt state of the gases, respectively the first and last cell of the computational domain. History of this expression (31) is monitored until it converges to the flame velocity, independently of the inlet velocity U_f [8].

The results obtained for $U_f = 0$ are compared with CANTERA reference computations in Fig. 1.a. The temperature and mass fractions profiles show an excellent agreement, including for the minor species H and HO₂, whose profiles in the flame appear indistinguishable from the reference.

The dependence of S_L with equivalence ratio is shown in Fig. 1.b, also showing a good agreement – below 10^{-3} relative error at $\varphi = 1$ – besides the important effective Lewis number variation for this range of equivalence ratio [59].

4.2. 2D Darrieus-Landau instability

To further demonstrate the capabilities of our model, let us study the intrinsic instability of the very flame presented above. The pseudo one-dimensional computational domain is now extended to a fully two-dimensional

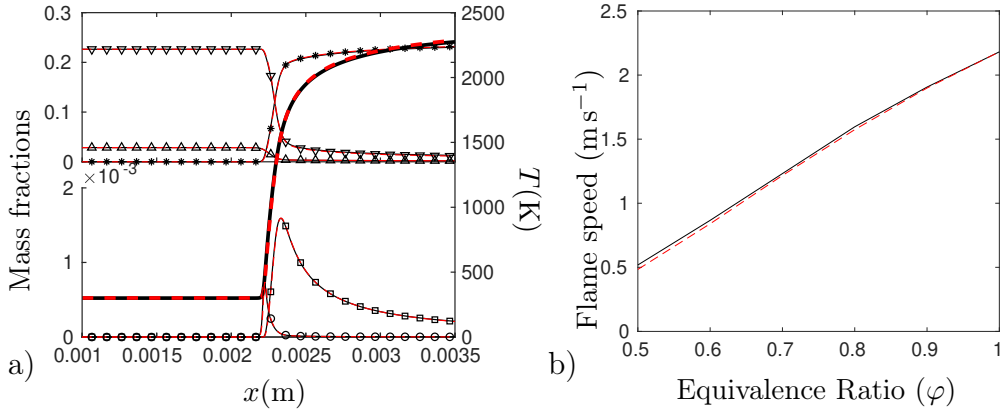


Figure 1: Freely propagating flame: a) Temperature profile (thick line), H_2 (Δ), O_2 (∇), H_2O ($*$), H (\square), HO_2 (\circ) mass fractions. Fresh gases are in stoichiometric proportion, at 300K and atmospheric pressure. b) Variation with equivalence ratio of the corresponding flame speed. CANTERA reference (plain line), and present model (red dashed line).

domain with grid size of 10^{-5} m. At $t = 0$, the 2D domain is initialized with the profiles obtained from the 1D computation reported in Fig. 1.a. The front position, defined as the maximum temperature gradient position is then perturbed with a wavenumber (k) of $600m^{-1}$. The evolution of the front position is reported in Fig. 2.a.

Qualitatively, it is interesting to note that the evolution produces the expected behavior, and that the coupling between the LB and FD solvers is robust to more complex flame front shapes. More quantitatively, Figure 2.b concludes the validation of this test case by comparing the growth rate in the linear regime with the analytical solution [40–42]. As expected, the amplitude A of the perturbation grows exponentially from its initial value A_0 according to

$$A = A_0 e^{\omega t}, \quad (32)$$

with ω the perturbation growth rate. Theory indicates that, in the linear

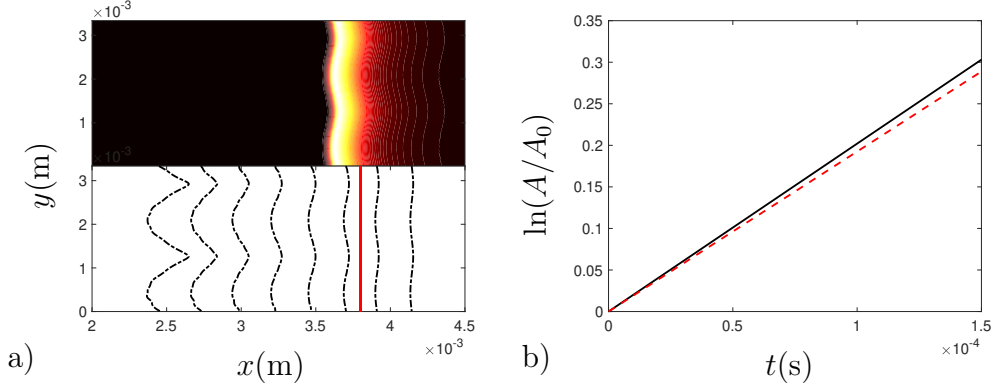


Figure 2: 2-D Darrieus Landau instability. a) Representation of the expansion with interval $\delta t = 10^{-4}$ s and $k = 600\text{m}^{-1}$. The front is initially at $x \approx 4.5\text{mm}$. The vertical line marks the end of the linear regime depicted in plot b. b) Comparison of analytical (solid line) and simulated growth rate (dashed line) in the linear region delimited ending at the vertical line in plot a.

regime [40–42],

$$\omega = S_L k \frac{-\sigma + \sqrt{\sigma^3 + \sigma^2 - \sigma}}{\sigma + 1}, \quad (33)$$

with k the wave number and $\sigma = \rho_f/\rho_b = 6.822$ the ratio between the fresh and burnt gases density.

4.3. Flame-vortex interaction

Let us conclude the validation of the model for premixed combustion by testing the classical flame-vortex interaction.

For this study, we will consider the propane-air single-step chemistry $\text{C}_3\text{H}_8 + 5\text{O}_2 \rightarrow 3\text{CO}_2 + 4\text{H}_2\text{O}$ detailed in our previous study [8]. Parameters for the thermodynamic closure are the classical NASA polynomials [60], and all species are assigned unity Lewis numbers

$$Sc_k = Pr = 0.682, \quad \forall k. \quad (34)$$

A two-dimensional $4\text{mm} \times 2\text{mm}$ domain is discretized ($\delta x = 10^{-5}\text{m}$) and initialized with the results of a planar premixed flame computation at equivalence ratio 0.8, corresponding to an expansion ratio of $\frac{\rho_f}{\rho_b} = 7.16$. The pre-exponential factor is adjusted to obtain a flame speed of $s_L = 0.5\text{m/s}$ and a flame thickness of $\delta_L = 0.25\text{mm}$. Next, two counter rotational vortices are added to the flow-field upstream of the planar flame as

$$\begin{cases} u_x &= U_0 - \epsilon \left(\frac{y-y_0}{R_0} \right) \exp \left(- \frac{(x-x_0)^2 + (y-y_0)^2}{2R_0^2} \right), \\ u_y &= \epsilon \left(\frac{x-x_0}{R_0} \right) \exp \left(- \frac{(x-x_0)^2 + (y-y_0)^2}{2R_0^2} \right), \end{cases} \quad (35)$$

where ϵ is the vortex strength, R_0 the characteristic radius and (x_0, y_0) are the coordinates of the vortex center. Three values of the vortex strength $\epsilon = (5, 30, 65)$ were adopted, corresponding to weak, moderate and strong interactions – referred hereafter as cases A, B and C. The initial distance of the vortex center to flame is 0.5mm ($= 2\delta_L$) at $t = 0$. A summary of the initialization setup is provided in the sketch of Fig. 3.

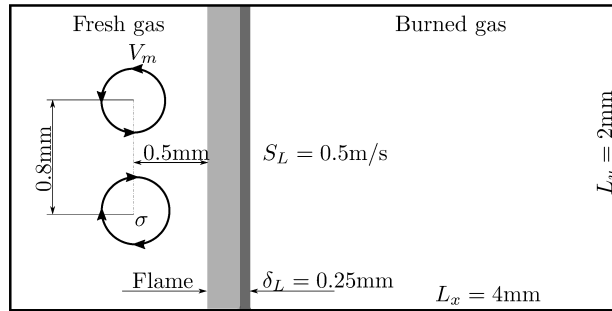


Figure 3: Numerical set-up for the the premixed flame / vortex interaction simulations.

To characterize the three regimes (A, B and C), we measure the following parameters at the instant the vortices start interacting with the flame:

- $\frac{V_m}{s_L}$, with V_m the effective vortex strength,
- $\frac{\sigma}{\delta_L}$, with σ the effective vortex radius.

Following [44], the Karlowitz number is defined as the ratio of these quantities

$$Ka = \frac{V_m \delta_L}{s_L \sigma}. \quad (36)$$

The effective vortex strength, radius and Karlowitz number for the three cases are reported in Table 1.

	V_m/s_L	σ/δ_L	Ka
Case A	3.80	1.32	2.88
Case B	20.00	1.16	17.24
Case C	52.00	1.12	46.43

Table 1: Effective vortex strength, radius and Karlowitz number for the three configurations (A, B and C) of vortex – flame interaction.

Figure 4 presents the temperature contours as obtained with our model at two successive instants (with the time normalized by δ_L/s_L). Accordingly, each case leads to very different topologies of interaction:

Case A Flame wrinkling appears and decays as the vortex intensity decreases.

Case B Moderate interaction leads to the formation of an unburnt gas pocket, which detaches and burns at a later time.

Case C For strong vortices, a significant elongation of the unburnt region appears into the burnt gases, before eventually separating and burning.

These observations are in line with the results reported in the literature [43–47].

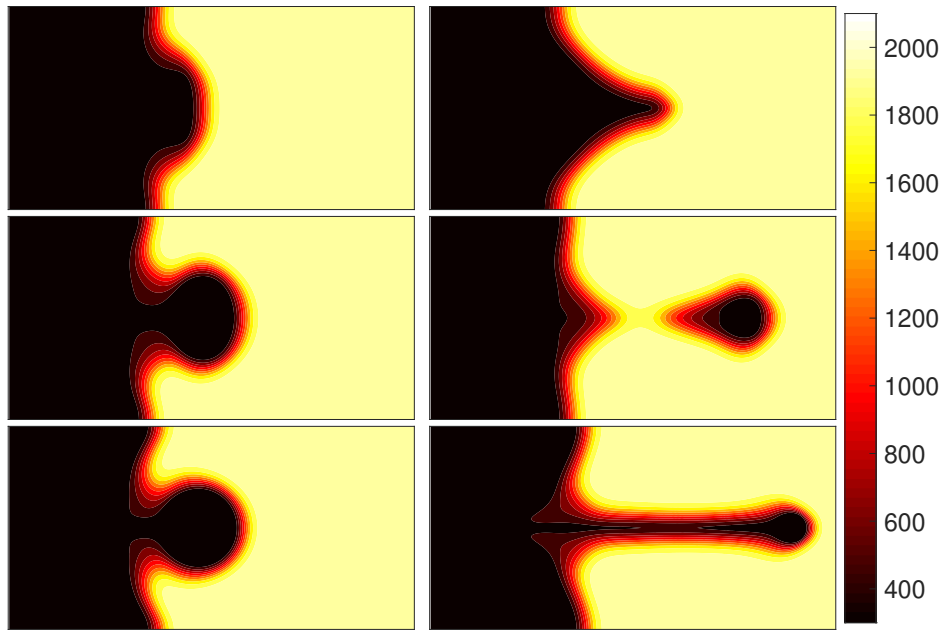


Figure 4: Contours of the temperature in a premixed flame - vortex interaction. From top to bottom: case A at $t= 2.12$ and $t=2.83$; case B at $t=1.42$ and $t=1.80$; case C at $t=0.90$ and $t=1.09$.

5. Non-premixed combustion in a double mixing layer

5.1. Design and numerical set-up of the test case

To illustrate the potential of the method, an ad-hoc test case illustrated in Fig. 5 was adapted from the athermal test case presented in [52] to show the stability of the collision model derived in Sec. 3.2. Doubly periodic shear

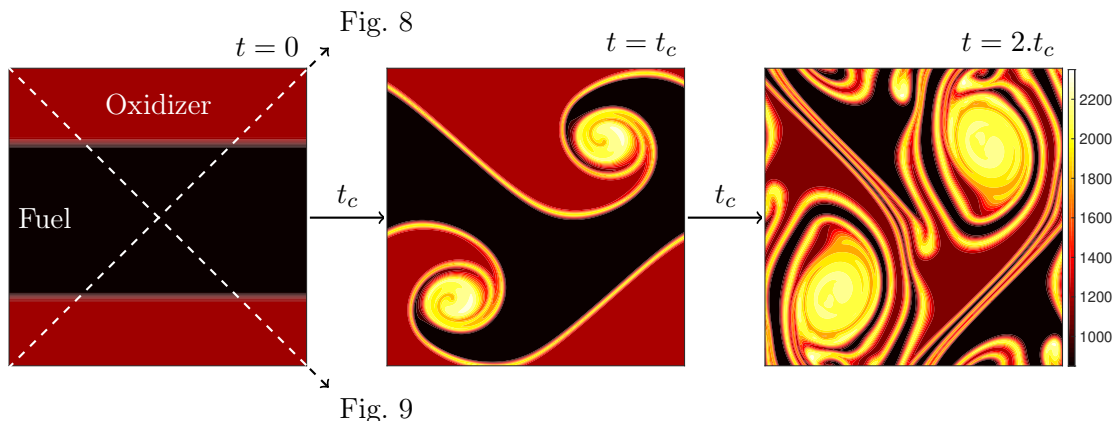


Figure 5: Temperature contours for the double shear layer configuration at $t = 0$, $t = t_c$, $t = 2.t_c$. The lines along which are plotted the profiles of Figs. 8 and 9 are indicated on the initial condition.

layer appeared to be a reasonable choice as it is known to be challenging to LB collision kernels [52], the classical BGK model almost always leading to failure.

For the results to resemble the incompressible test case presented in [52], we decided to keep the same initial velocity field, Reynolds number (30000) and momentum ratio between the streams. Next, we set the initial temperature and composition of the two streams so that a diffusion flame would auto-ignite and stabilize in between (e.g. one oxidizer and one fuel stream, as shown in Fig. 5). This test case was imagined to be as close as can be to a jet diffusion flame, whilst keeping simple (periodic) boundary conditions.

Under these considerations, we considered a $[0, L] \times [0, L]$ 2D domain, with $L = 5\text{cm}$, in which initial conditions are fully defined through

$$\left\{ \begin{array}{l} u_x(x, y) = U_0 \tanh\left(\lambda\left(\frac{1}{4} - \left|\frac{y}{L} - \frac{1}{4}\right|\right)\right) \\ u_y(x, y) = \epsilon U_0 \sin\left(2\pi\left(\frac{x}{L} + \frac{1}{4}\right)\right), \\ p(x, y) = p_0 \\ \rho(x, y) = \rho_0, \\ Y_{\text{H}_2}(x, y) = Y_{\text{H}_2}^F \left(1 + \tanh\left(\lambda\left(\frac{1}{4} - \left|\frac{y}{L} - \frac{1}{4}\right|\right)\right)\right) / 2, \\ Y_{\text{O}_2}(x, y) = Y_{\text{O}_2}^O \left(1 - \tanh\left(\lambda\left(\frac{1}{4} - \left|\frac{y}{L} - \frac{1}{4}\right|\right)\right)\right) / 2, \\ Y_{\text{N}_2}(x, y) = 1 - Y_{\text{H}_2}(x, y) - Y_{\text{O}_2}(x, y), \end{array} \right. \quad (37)$$

corresponding to the smooth profiles illustrated in the first contour of Fig. 5, using the parameters summarized in Tab. 2. Note that use of these parameters leads to a temperature of $T^F = 853\text{K}$ in the fuel stream and $T^O = 1200\text{K}$ in the oxidizer stream. Using the fuel stream conditions, and following the

$Y_{\text{H}_2}^F$	28.5×10^{-3}
$Y_{\text{O}_2}^O$	266×10^{-3}
U_0	96 m s^{-1}
p_0	$101\,325 \text{ Pa}$
ρ_0	0.2926 kg m^{-3}
ϵ	0.05
λ	80

Table 2: Physical parameters for the double shear layer test case.

definition proposed in [52], the Reynolds number can be obtained as

$$Re = \frac{\rho_0 U_0 L}{\mu} = 30\,000, \quad (38)$$

using the fuel stream parameters from Table 2, and the viscosity obtained from (B.2) at T^F . Note that the alternative value of 37 300 may be obtained

based on the less viscous oxidizer stream. It is also useful for the discussion to define the convective time t_c as

$$t_c = \frac{L}{U_0}, \quad (39)$$

The flow evolution was simulated up to $2t_c$ on a 1024^2 cartesian grid, using both our hybrid LB solver and the DNS solver NTMIX [61], leading to the temperature contours displayed in the second and third plots of Fig. 5.

NTMIX is an in-house parallel DNS flow solver developed at CERFACS, Toulouse. Space is discretized through 6^{th} or 8^{th} order centered finite differences schemes, and time integration is performed with a 3^{rd} order Runge-Kutta. NTMIX is coupled with a CHEMKIN version for the computation of transport, thermodynamics and kinetics properties. The simulations conducted for this work use the 8^{th} order discretization, mixture-averaged transport properties [62], the 12-step H₂-air chemistry [26], and neglect the Soret effect.

For the results to be comparable with both codes, the pressure term in (11) $\frac{Dp}{Dt}$ was approximated as $\frac{\partial p}{\partial t}$, as to obtain a good agreement on the pressure and temperature fields in this confined configuration.

5.2. Validation of the velocity field

In order to validate the flow-field, we successively simulated the cold-flow (e.g. without kinetic source term) and the reacting flow. Figure 6 presents vorticity contours after one convective time $t = t_c$, showing excellent qualitative agreement. Let us now confirm this validation quantitatively by plotting the profiles along the diagonal lines of the domain identified in Fig.

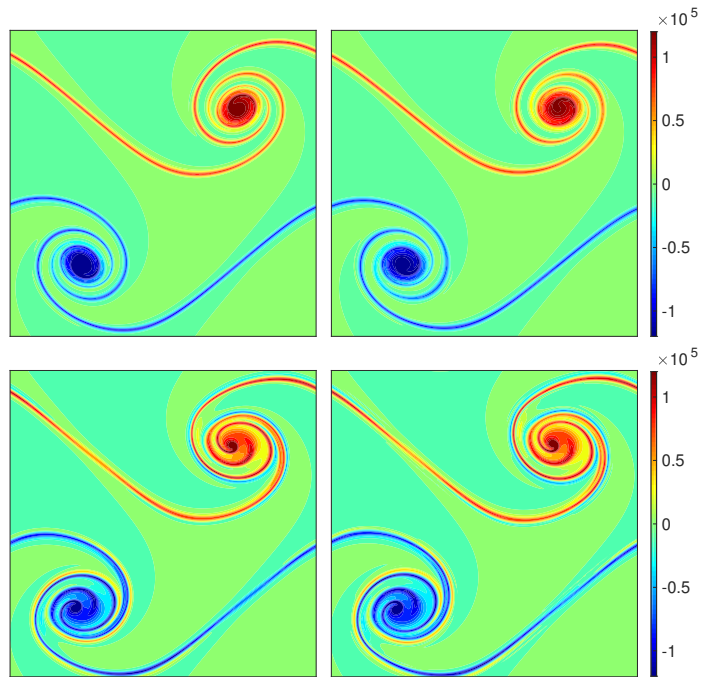


Figure 6: Doubly periodic shear layer at $Re = 3.10^4$. Vorticity contours (magnitude of the z-component) at $t = t_c$. NTMIX contours (left) compared with the LBM contours (right), for the compressible “cold” flow (top) and the “hot” flow (bottom), e.g. including the chemical source term, on a 1024×1024 grid.

5. This is done in Fig. 7: for each simulation, we plotted both velocity components (u_x, u_y) – easily distinguishable given the flow configuration – both for the cold and hot test case, and at two successive convective times ($t = t_c, t = 2t_c$). Superimposed in light gray is the domain diagonal along

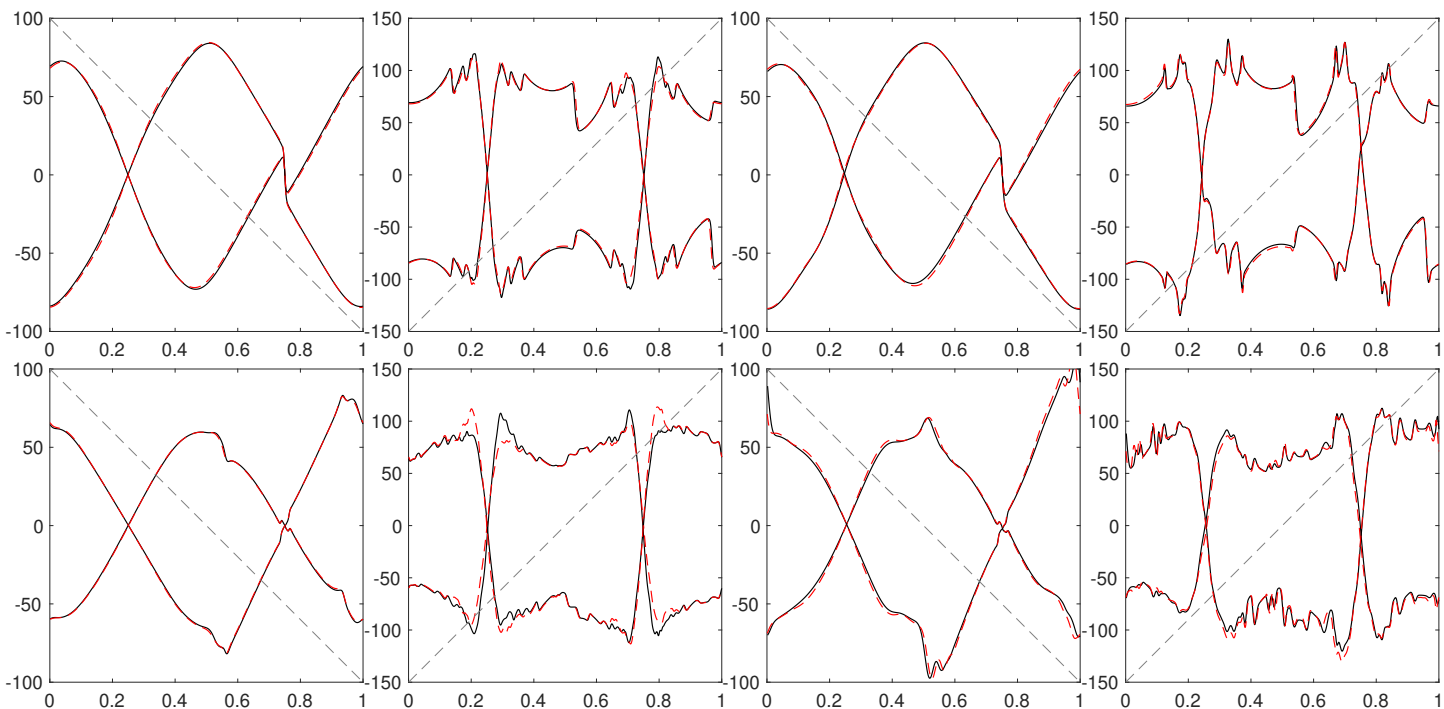


Figure 7: Velocity profiles (m s^{-1}) at $t = t_c$ (top) and $t = 2t_c$ (bottom) as obtained with NTMIX (solid line) and LB solver (dashed line) along the diagonal lines superimposed as illustrated in Fig. 5, for the cold (left) and hot (right) case.

which the profile is plotted. Besides small discrepancies appearing at $2t_c$, the agreement is overall excellent, hereby confirming the results of Fig.6.

5.3. Reacting flow validation

Let us now focus on the reactive case. Figures 8 and 9 present profiles of temperature, as well as H_2 , H and H_2O mass fractions along the two domain diagonals. Again, agreement along the diagonal passing through the

two vortices (Fig. 8) is seen to be excellent after both one and two convective times. The profiles on the second diagonal (Fig. 9) are equally good after one

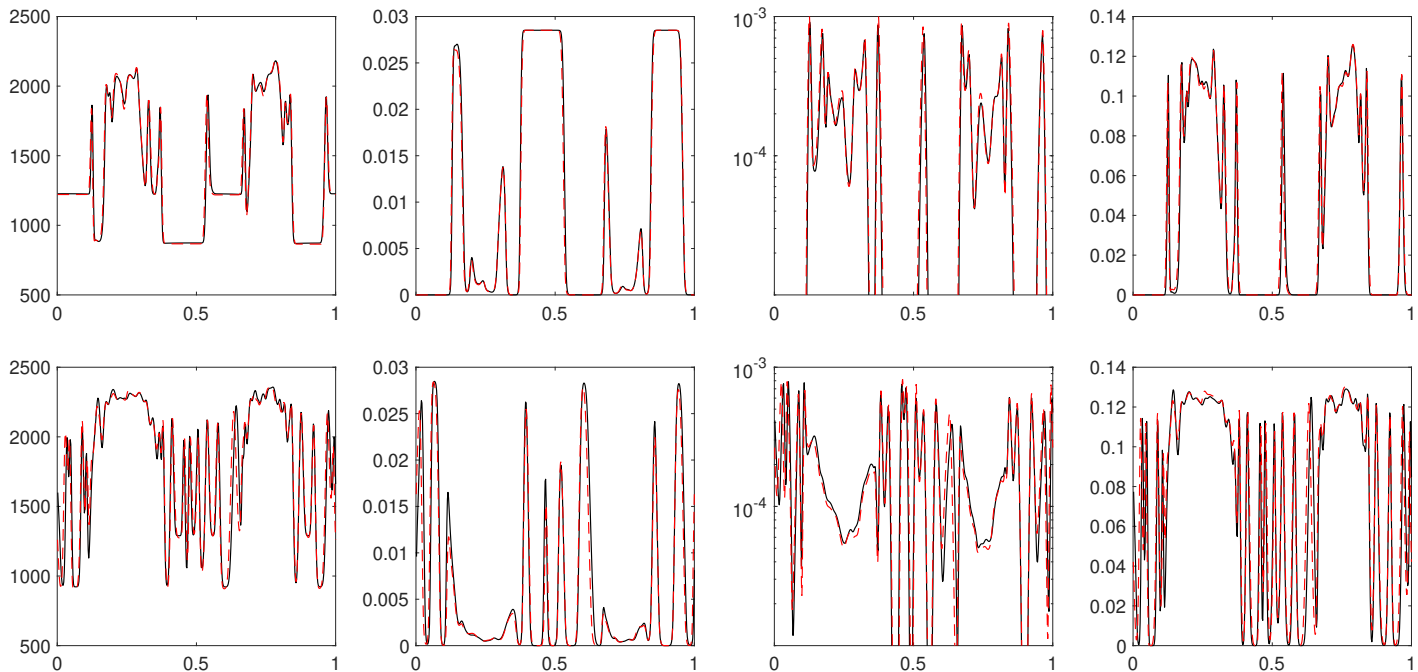


Figure 8: Temperature (K), Y_{H_2} , Y_H and Y_{H_2O} (from left to right) profiles as obtained with NTMIX (solid line) and LB solver (dashed line) along the diagonal identified in Fig. 5, after one (top) and two (bottom) convective times.

convective time, but start showing discrepancies at two convective times. The authors believe those departures to be explained by three factors, in order of likelihood:

1. Any small error on the flow leads to significant errors on this axis since the vorticity contour is almost aligned with the profile line, as clearly visible in the second plot of Fig. 5.
2. The pressure work is of prime importance in this configuration. Approximating $\frac{Dp}{Dt}$ as $\frac{\partial p}{\partial t}$ in (11) may be too stark after two convective

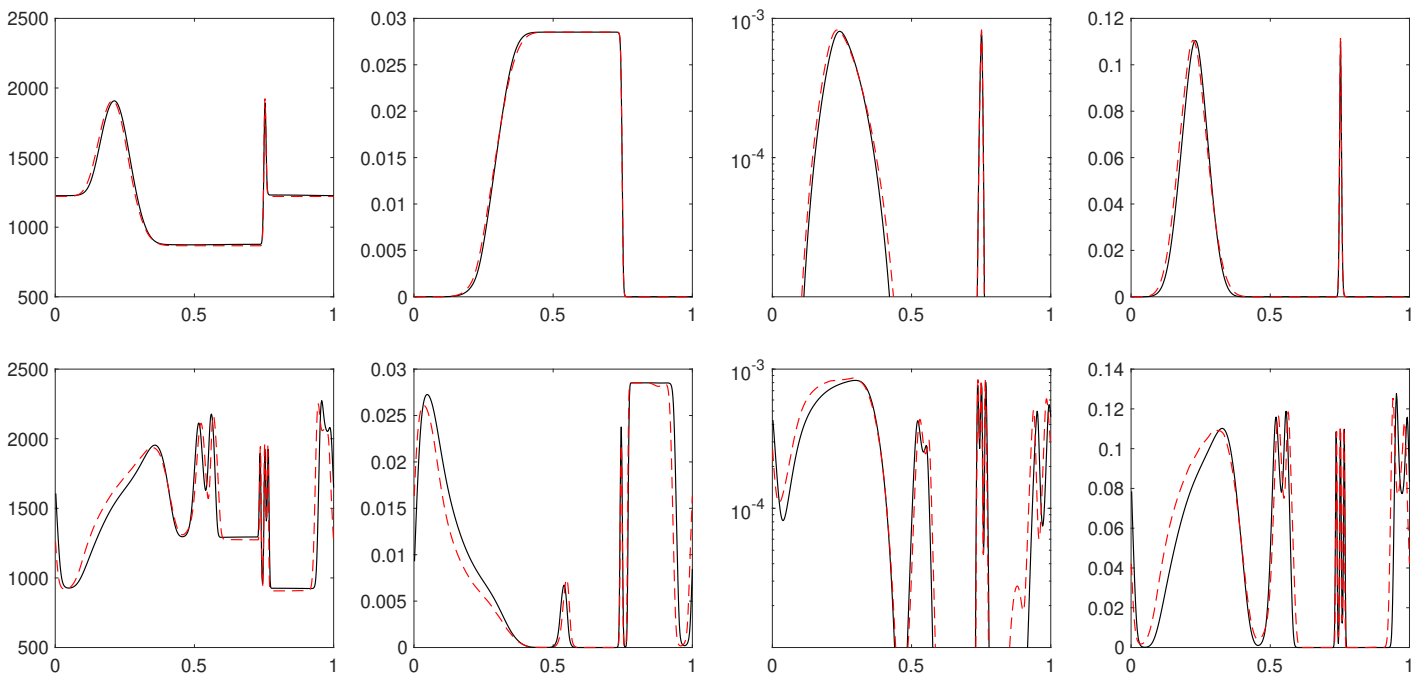


Figure 9: Temperature (K), Y_{H_2} , Y_H and Y_{H_2O} (from left to right) profiles as obtained with NTMIX (solid line) and LB solver (dashed line) along the diagonal identified in Fig. 5, after one (top) and two (bottom) convective times.

times.

3. Transport models are different in both solver: constant Lewis numbers are assumed in the LB solver, whereas NTMIX solver assumes mixture-averaged properties.

Factor 1, in our opinion, is responsible for most of the departure appearing in Fig. 9 after two convective times. The agreement remains, however, very good for the Lattice-Boltzmann simulation of such a complex reactive flow configuration.

6. Robustness, accuracy and computational cost

Let us conclude this study by a discussion on robustness and accuracy. Figure 10 shows the relative error obtained for the flame velocity of Fig. 1 as a function of the number of point per flame thickness. Here, we have defined

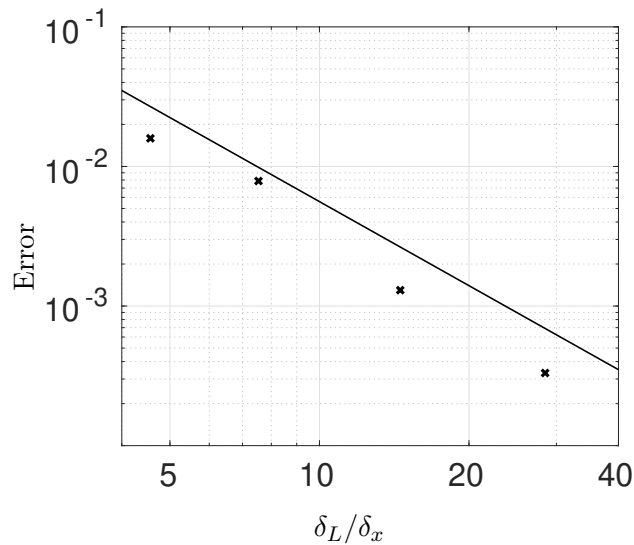


Figure 10: Relative error on the flame velocity as a function of the number of point per flame thickness δ_L

the flame thickness as

$$\delta_L = \frac{T_b - T_f}{\max \left| \frac{\partial T}{\partial x} \right|}, \quad (40)$$

with T_f and T_b the temperature of the fresh and the burnt gases, respectively, as given in Tab. B.5. The reference for the error is the velocity as obtained on an over-refined 2000 points grid – which we found to be less than 0.1% off the CANTERA result presented in Fig. 1.a. Note that, following this definition, the profiles of Fig. 1.a corresponds to $\frac{\delta_L}{\delta_x} = 16$ points per flame thickness.

As identified by the line, the convergence is second-order with the spatial discretization. This result is surprising, since the convection term is a simple second-order central difference scheme including 10% of upwinding (which should degrade the order of accuracy), and that the solvers coupling is first-order. Note, however, that most test cases do not require any upwinding, and that the diffusion scheme is second-order. We have also tested higher-order schemes for the convection term and the FD temporal integration, without appreciable difference in the convergence. This seems to indicate that the obtained solver mostly keeps the low-dissipation feature characteristic of LB methods [31, 58].

Another interesting result to be noted from Fig. 10 is the robustness of the method: the algorithm does converge even with only 5 points in the flame, an excellent result considering the stiffness of the $\text{H}_2 - \text{O}_2$ chemistry – confirmed by the sharpness of the intermediate species in Fig. 1.

To further assess the robustness of the method, we ran again the double shear layer while reducing the number of grid points. Figure 11 presents comparisons of the vorticity contours obtained by repeating Fig. 6 on 512^2 ,

256² and 128² grids. They all show convergence, despite the inevitable loss of accuracy of the gradients. Note that the reference DNS fails to converge on the 256² and 128² grids as the small scales become under-resolved. A detailed

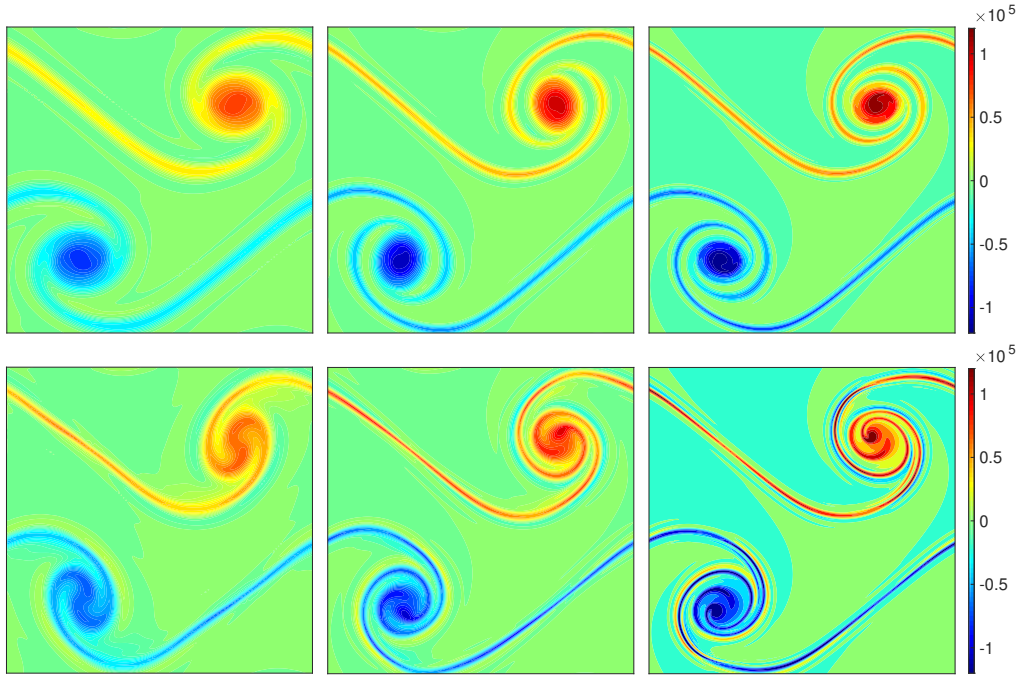


Figure 11: Vorticity contours in the cold (top) and hot (bottom) double shear layer, for different grids. From left to right: 128 \times 128, 256 \times 256, and 512 \times 512.

assessment of our collision kernel associated hyper-viscosity, responsible for this robustness, will be carefully conducted in future works.

To close this Section, let us add a note on the computational cost involved, which may serve as perspective for practical Large Eddy Simulations applications [63]. In human time, computing one convective time – or 15000 time steps – of the reactive flow on the 1024 \times 1024 grids takes about 1.1 hours on a 20-core Ubuntu desktop (2 \times Intel Xeon(R) CPU E5-2630 v4 2.20GHz). This result is encouraging: it corresponds to 5.1 μ s per grid point, which,

assuming perfect scaling translates to less than 150 000 / cpuh to run 10^6 time-steps on 10^8 grid points.

Use of the hybrid regularized collision model costs a mere 15% more than the conventional single relaxation time (SRT) model, which only provides the required stability for the planar premixed flame propagation presented in Fig. 1. We also measured the relative cost of the cold and hot flow simulation with the athermal simulation (e.g. $\theta \equiv 1$, and no finite difference solver). Figures are presented in Table 3. These results will be improved in the future as no

Flow model	Cost
Athermal flow	1
Cold flow	2.77
Hot flow	3.63

Table 3: Relative computational costs of the method on the double shear layer. Athermal flow : as in [29]; Cold flow: PR collision with the transport equations for energy and 9 species; Hot flow: cold flow configuration plus chemical sources evaluated using the 12-step chemistry.

optimization of any kind was performed on the FD solver at this stage, but are certainly promising: including a relatively simple chemistry adds about 30% computational cost, indicating a wide margin for progress. Also, the ratio of the reacting simulation cost to the athermal flow is quite classical, indicating that gains in cpu costs obtained in aerodynamics and aeroacoustics [2–6] may be obtained in the field of combustion in the near future.

7. Concluding remarks

A new hybrid Lattice-Boltzmann model for low-Mach reactive flows was presented following [8]. Mass and momentum conservation are addressed

within a Lattice-Boltzmann solver, whereas the energy and species conservation are addressed via a classical finite difference solver.

To cope with the limitations of the standard BGK collision model [1], an ad-hoc model was presented as an extension to thermal multicomponent flows of Jacob et al's proposal [29].

We then presented major progress compared to our initial proposal [8]: not only does the present work lift the constant C_p and single step chemistry assumptions, but stability and robustness are tested on challenging two-dimensional flows.

The final discussion on accuracy, robustness and cpu cost clearly opens the door to Large Eddy Simulation in that context. Future work will include a detailed account on the model numerical viscosity as to allow the simulation of 3D flames in turbulent flows by inclusion of a turbulence model.

Acknowledgements

B. Cuenot is gratefully acknowledged for fruitful discussions and providing the NTMIX code (and A. Pestre for helping setting up the NTMIX computations). J. Jacob provided invaluable help with the implementation. P. Haldenwang is gratefully acknowledged for fruitful discussions on thermo-diffusive instabilities.

The French Space agency (CNES) is acknowledged for supporting Song Zhao at M2P2. This work was granted access to the HPC resources of Aix-Marseille Université funded by the project Equip@Meso (ANR-10-EQPX-29-01), and from GENCI-TGCC/CINES (Grant 2018-A0032A07679). We also acknowledge support from Labex MEC (ANR-10-LABX-0092) and the

A*MIDEX project (ANR-11-IDEX-0001-02), funded by the “Investissements d’Avenir”.

Appendix A. Chapman-Enskog expansion

The CE expansion of equation (1) is performed in the Hermite polynomial space [53]. The Hermite tensor applied in the current study at order n reads

$$\mathcal{H}_{\alpha_1 \dots \alpha_n}^{(n)}(\boldsymbol{\xi}) \equiv \frac{(-r_0 T_0)^n}{\omega(\boldsymbol{\xi})} (\partial_{\alpha_1} \dots \partial_{\alpha_n} \omega(\boldsymbol{\xi})) , \quad (\text{A.1})$$

and the weight function $\omega(\boldsymbol{\xi})$ is defined as

$$\omega(\boldsymbol{\xi}) \equiv \frac{1}{(2\pi c_s^2)^{D/2}} \exp\left(-\frac{\boldsymbol{\xi}^2}{2c_s^2}\right), \quad (\text{A.2})$$

with $\xi^2 \equiv \boldsymbol{\xi} \cdot \boldsymbol{\xi}$ and c_s the reference speed of sound

$$c_s \equiv \sqrt{r_0 T_0} . \quad (\text{A.3})$$

where r_0, T_0 are the reference gas constant and reference temperature respectively. It is worth noting that compared to weight functions used in thermal LBMs [53, 54], a reference gas constant is introduced to overcome the difficulties brought out by the non-constant molecular weights of the gas mixture. The VDF f can be projected to its Hermite coefficients tensor through

$$a_{\alpha_1 \dots \alpha_n}^{(n)}(\mathbf{x}, t) \equiv \int f(\mathbf{x}, \boldsymbol{\xi}, t) \mathcal{H}_{\alpha_1 \dots \alpha_n}^{(n)}(\boldsymbol{\xi}) d\boldsymbol{\xi} . \quad (\text{A.4})$$

According to the orthogonality of Hermite polynomials, the VDF can be projected back from the Hermite space via

$$f(\mathbf{x}, \boldsymbol{\xi}, t) = \omega(\boldsymbol{\xi}) \sum_{n=0}^{\infty} \frac{1}{(n)! c_s^{2n}} \mathbf{a}^{(n)}(\mathbf{x}, t) : \mathcal{H}^{(n)}(\boldsymbol{\xi}), \quad (\text{A.5})$$

where the operator $(:)$ stands for full contraction of two tensors. Applying the projection (A.4) to the equilibrium distribution (2), the equilibrium coefficient tensors provided in Eq. (21) are obtained.

Projecting equation (1) to the Hermite space, one has

$$\frac{\partial}{\partial t} a_{\alpha_1 \dots \alpha_n}^{(n)} + \frac{\partial}{\partial x_j} (\xi_j a_{\alpha_1 \dots \alpha_n}^{(n)}) = -\frac{1}{\tau} (a_{\alpha_1 \dots \alpha_n}^{(n)} - a_{\alpha_1 \dots \alpha_n}^{(n), \text{eq}}) \quad (\text{A.6})$$

Note that the index j repeats from 1 to D (the spatial dimension). Using the Rodrigues recursive relation of the Hermite tensor

$$\xi_j \mathcal{H}_{\alpha_1 \dots \alpha_n}^{(n)}(\boldsymbol{\xi}) = \mathcal{H}_{j\alpha_1 \dots \alpha_n}^{(n+1)}(\boldsymbol{\xi}) + c_s^2 \sum_{i=1}^n \delta_{j\alpha_i} \mathcal{H}_{\alpha_1 \dots \alpha_{i-1} \alpha_{i+1} \dots \alpha_n}^{(n-1)}(\boldsymbol{\xi}), \quad (\text{A.7})$$

equation (A.6) becomes

$$\partial_t a_{\alpha_1 \dots \alpha_n}^{(n)} + \partial_j \left(a_{j\alpha_1 \dots \alpha_n}^{(n+1)} \right) + c_s^2 \sum_{i=1}^n \left(\partial_{\alpha_i} a_{\alpha_1 \dots \alpha_{i-1} \alpha_{i+1} \dots \alpha_n}^{(n-1)} \right) = -\frac{1}{\tau} (a_{\alpha_1 \dots \alpha_n}^{(n)} - a_{\alpha_1 \dots \alpha_n}^{(n), \text{eq}}). \quad (\text{A.8})$$

The CE analysis is performed on this equation. The scale separation respect to Knudsen number ϵ is achieved by setting the operator

$$\partial_t = \epsilon \partial_{t_1} + \epsilon^2 \partial_{t_2}; \quad \partial_j = \epsilon \partial_{j_1}, \quad (\text{A.9})$$

and the coefficients tensor

$$\mathbf{a}^{(n)} = \mathbf{a}^{(n), \text{eq}} + \mathbf{a}^{(n), 1}, \quad \text{where } \mathbf{a}^{(n), 1} / \mathbf{a}^{(n), \text{eq}} \sim \mathcal{O}(\epsilon) \ll 1. \quad (\text{A.10})$$

It is worth noting that $a^{(0), 1} = a_{\alpha}^{(1), 1} = 0$ according to equation (5). Inserting (A.9) and (A.10) into (A.6), the system can be written at different

orders of ϵ as

$$\epsilon \partial_{t_1} a_{\alpha_1 \dots \alpha_n}^{(n), \text{eq}} + \epsilon \partial_{j_1} \left(a_{j \alpha_1 \dots \alpha_n}^{(n+1), \text{eq}} \right) + c_s^2 \sum_{i=1}^n \left(\epsilon \partial_{\alpha_{i_1}} a_{\alpha_1 \dots \alpha_{i-1} \alpha_{i+1} \dots \alpha_n}^{(n-1), \text{eq}} \right) = -\frac{1}{\tau} a_{\alpha_1 \dots \alpha_n}^{(n), 1} \quad \sim \mathcal{O}(\epsilon^1) \quad (\text{A.11a})$$

$$\epsilon^2 \partial_{t_2} a_{\alpha_1 \dots \alpha_n}^{(n), \text{eq}} + \epsilon \partial_{t_1} a_{\alpha_1 \dots \alpha_n}^{(n), 1} + \epsilon \partial_{j_1} \left(a_{j \alpha_1 \dots \alpha_n}^{(n+1), 1} \right) + c_s^2 \sum_{i=1}^n \left(\epsilon \partial_{\alpha_{i_1}} a_{\alpha_1 \dots \alpha_{i-1} \alpha_{i+1} \dots \alpha_n}^{(n-1), 1} \right) = 0 \quad \sim \mathcal{O}(\epsilon^2) \quad (\text{A.11b})$$

$$\epsilon^2 \partial_{t_2} a_{\alpha_1 \dots \alpha_n}^{(n), 1} = 0 \quad \sim \mathcal{O}(\epsilon^3) \quad (\text{A.11c})$$

Summing all the orders together and using the expression of the equilibrium coefficients in equation (21), the following relationships are achieved

$$\partial_t \rho + \partial_\alpha (\rho u_\alpha) = 0, \quad (\text{A.12a})$$

$$\partial_t (\rho u_\alpha) + \partial_\beta (\rho u_\alpha u_\beta + p \delta_{\alpha\beta}) = -\partial_\beta a_{\alpha\beta}^{(2), 1}, \quad (\text{A.12b})$$

$$\begin{aligned} & \partial_t (\rho u_\alpha u_\beta + p \delta_{\alpha\beta} - \rho r_0 T_0 \delta_{\alpha\beta}) + \partial_\gamma [\rho u_\gamma u_\alpha u_\beta + (p - \rho r_0 T_0) (\mathbf{u}\boldsymbol{\delta})_{\gamma\alpha\beta}] \\ & + c_s^2 [\partial_\alpha (\rho u_\beta) + \partial_\beta (\rho u_\alpha)] + \partial_t a_{\alpha\beta}^{(2), 1} + \partial_\gamma a_{\gamma\alpha\beta}^{(3), 1} = -\frac{1}{\tau} a_{\alpha\beta}^{(2), 1}. \end{aligned} \quad (\text{A.12c})$$

Equation (A.12a) gives the mass conservation in (6). The next step is to find an explicit expression of $a_{\alpha\beta}^{(2), 1}$ to fulfill the viscous tensor in the momentum equation (A.12b). Using equations (A.12a) and (A.12b), the transport equation for $\rho u_\alpha u_\beta$ can be written as

$$\partial_t (\rho u_\alpha u_\beta) + \partial_\gamma (\rho u_\alpha u_\beta u_\gamma) + (\partial_\alpha p) u_\beta + (\partial_\beta p) u_\alpha = -u_\beta \partial_\gamma a_{\alpha\gamma}^{(2), 1} - u_\alpha \partial_\gamma a_{\beta\gamma}^{(2), 1}. \quad (\text{A.13})$$

Inserting back to (A.12c),

$$\delta_{\alpha\beta} [\partial_t p + \partial_\gamma (u_\gamma p)] + 2p S_{\alpha\beta} - u_\beta \partial_\gamma a_{\alpha\gamma}^{(2), 1} - u_\alpha \partial_\gamma a_{\beta\gamma}^{(2), 1} + \partial_t a_{\alpha\beta}^{(2), 1} + \partial_\gamma a_{\gamma\alpha\beta}^{(3), 1} = -\frac{1}{\tau} a_{\alpha\beta}^{(2), 1}, \quad (\text{A.14})$$

where $S_{\alpha\beta} \equiv \frac{1}{2}(\partial_\beta u_\alpha + \partial_\alpha u_\beta)$ is the strain-rate tensor. Omitting the $\mathcal{O}(\epsilon)$ terms in the above equation, the viscous tensor appears in the momentum equation (A.12b) as

$$a_{1,\alpha\beta}^{(2)} = -2p\tau S - \tau\delta_{\alpha\beta} [\partial_t p + \partial_\gamma(u_\gamma p)], \quad (\text{A.15})$$

with the second term being negligible in the low Mach approximation. Setting

$$\tau = \frac{\mu}{p}, \quad (\text{A.16})$$

then leads to recovery of the viscous tensor in equation (8). Note that, unlike with mono-species thermal LBM, the second term in equation (A.15) can not be linked to the bulk viscosity using the energy conservation for mono-species $\partial_t \theta + u_\gamma \partial_\gamma \theta + \frac{2}{D}\theta \partial_\gamma \theta = 0$, because this energy equation is generally invalid for multi-species flow.

Appendix B. Thermochemistry & transport

H₂-air combustion model

Throughout the paper, we consider the 12-step skeletal mechanism for H₂-air combustion [26] derived from the detailed San Diego mechanism [27]. The mechanism, summarized in Tab.B.4, involves eight reacting species, as well as inert N₂ for combustion with air. The associated thermodynamic data was obtained from the San Diego mechanism website [27].

Thermodynamic closure

The thermodynamic properties required for the thermodynamic closure are specified in the form of the classical NASA polynomials [23] for each

1	$\text{H} + \text{O}_2 \rightleftharpoons \text{OH} + \text{O}$	7	$\text{HO}_2 + \text{OH} \rightarrow \text{H}_2\text{O} + \text{O}_2$
2	$\text{H}_2 + \text{O} \rightleftharpoons \text{OH} + \text{H}$	8	$\text{H} + \text{OH} + \text{M} \rightleftharpoons \text{H}_2\text{O} + \text{M}$
3	$\text{H}_2 + \text{OH} \rightleftharpoons \text{H}_2\text{O} + \text{H}$	9	$2 \text{H} + \text{M} \rightleftharpoons \text{H}_2 + \text{M}$
4	$\text{H} + \text{O}_2 + \text{M} \rightarrow \text{HO}_2 + \text{M}$	10	$2 \text{HO}_2 \rightarrow \text{H}_2\text{O}_2 + \text{O}_2$
5	$\text{HO}_2 + \text{H} \rightarrow 2 \text{OH}$	11	$\text{HO}_2 + \text{H}_2 \rightarrow \text{H}_2\text{O}_2 + \text{H}$
6	$\text{HO}_2 + \text{H} \rightleftharpoons \text{H}_2 + \text{O}_2$	12	$\text{H}_2\text{O}_2 + \text{M} \rightarrow 2 \text{OH} + \text{M}$

Table B.4: The 12-step skeletal mechanism for the combustion of H₂-air [26]. Up-to-date rates are available [27].

species k . Computation of the temperature is done through a Newton iterative procedure with the previous time-step temperature as initial condition. Considering this thermodynamic closure, the thermodynamic equilibrium, required to initialize the premixed flame presented in Fig. 1, is given in Table B.5.

Table B.5: Initial conditions: 1-D domain is initialized with fresh gases corresponding to $(0 : L/2)$ and burnt gases $(L/2 : L)$

<i>Variables</i>	fresh gases	burnt gases
T	300 K	2385 K
p	1 atm	1 atm
Y_{H_2}	2.852×10^{-2}	1.145×10^{-3}
Y_{H}	0	6.983×10^{-5}
Y_{O_2}	2.264×10^{-1}	7.474×10^{-3}
Y_{OH}	0	5.458×10^{-3}
Y_{O}	0	3.838×10^{-4}
$Y_{\text{H}_2\text{O}}$	0	2.403×10^{-1}
Y_{HO_2}	0	1.074×10^{-6}
$Y_{\text{H}_2\text{O}_2}$	0	1.444×10^{-10}
Y_{N_2}	7.451×10^{-1}	7.451×10^{-1}

Simplified transport model

The thermal diffusion coefficient, required in (12) is defined as

$$\lambda = \frac{\mu}{\text{Pr}} \sum_{k=1}^N Y_k C_{p,k}, \quad (\text{B.1})$$

with μ the dynamic viscosity, assumed here to follow temperature-dependent power-law

$$\mu = \mu_0 \left(\frac{T}{T_0} \right)^\beta. \quad (\text{B.2})$$

The diffusion velocities are evaluated through a Fickian approximation

$$V_{k,\alpha} = -D_k \frac{\partial X_k}{\partial x_\alpha} \frac{W_k}{\overline{W}} + V_\alpha^c Y_k, \quad (\text{B.3})$$

with X_k the k -th species mole fraction and D_k its diffusion coefficient, which is determined via the component specific Schmidt number Sc_k from the viscosity

$$D_k = \frac{\mu}{\rho \text{Sc}_k}. \quad (\text{B.4})$$

A correction velocity [49] is applied to ensure mass conservation, reading

$$V_\alpha^c = \sum_{k=1}^N D_k \frac{\partial X_k}{\partial x_\alpha} \frac{W_k}{\overline{W}}. \quad (\text{B.5})$$

The various parameters required for the computation of the viscosity through (B.2) as well as species (B.4) and heat (B.1) diffusion properties are those recommended in Cerfacs' database [64] and validated for this mechanism. They are reported in Tab. B.6.

References

- [1] S. Chen, G. D. Doolen, Lattice boltzmann method for fluid flows, Annual review of fluid mechanics 30 (1) (1998) 329–364.

μ_0	1.8405×10^{-5}	β	0.6759
Pr	0.7500	Sc_{H_2}	0.2100
Sc_H	0.1400	Sc_{O_2}	0.8000
Sc_{OH}	0.5300	Sc_O	0.5300
Sc_{H_2O}	0.6000	Sc_{HO_2}	0.8000
$Sc_{H_2O_2}$	0.8200	Sc_{N_2}	1.0000

Table B.6: Power-law's viscosity coefficients (SI units), Prandtl number and Schmidt numbers for each species of the 12-step mechanism.

- [2] A. D'Hooge, L. Rebbeck, R. Palin, Q. Murphy, J. Gargoloff, B. Duncan, Application of real-world wind conditions for assessing aerodynamic drag for on-road range prediction, Tech. rep., SAE Technical Paper (2015).
- [3] M. E. Gleason, B. Duncan, J. Walter, A. Guzman, Y.-C. Cho, Comparison of computational simulation of automotive spinning wheel flow field with full width moving belt wind tunnel results, SAE International Journal of Passenger Cars-Mechanical Systems 8 (2015-01-1556) (2015) 275–293.
- [4] M. R. Khorrami, E. Fares, B. Duda, A. Hazir, Computational evaluation of airframe noise reduction concepts at full scale, in: 22nd AIAA/CEAS Aeroacoustics Conference, 2016, p. 2711.
- [5] M. R. Khorrami, E. Fares, Simulation-based airframe noise prediction of a full-scale, full aircraft, in: 22nd AIAA/CEAS aeroacoustics conference, 2016, p. 2706.
- [6] D. Casalino, A. Hazir, A. Mann, Turbofan broadband noise prediction using the lattice boltzmann method, AIAA Journal (2017) 1–20.

- [7] G. Romani, D. Casalino, Rotorcraft blade-vortex interaction noise prediction using the lattice-boltzmann method, *Aerospace Science and Technology*.
- [8] Y. Feng, M. Tayyab, P. Boivin, A lattice-boltzmann model for low-mach reactive flows, *Combustion and Flame* 196 (2018) 249 – 254.
- [9] O. Filippova, D. Hänel, A Novel Lattice BGK Approach for Low Mach Number Combustion, *Journal of Computational Physics* 158 (2) (2000) 139–160.
- [10] K. Yamamoto, N. Takada, LB simulation on soot combustion in porous media, *Physica A: Statistical Mechanics and its Applications* 362 (1) (2006) 111–117.
- [11] E. Chiavazzo, I. V. Karlin, A. N. Gorban, K. Boulouchos, Coupling of the model reduction technique with the lattice Boltzmann method for combustion simulations, *Combustion and Flame* 157 (10) (2010) 1833–1849.
- [12] A. Xu, C. Lin, G. Zhang, Y. Li, Multiple-relaxation-time lattice boltzmann kinetic model for combustion, *Physical Review E* 91 (4) (2015) 043306.
- [13] K. Sun, S. Yang, C. K. Law, A diffuse interface method for simulating the dynamics of premixed flames, *Combustion and Flame* 163 (2016) 508–516.
- [14] M. Ashna, M. H. Rahimian, A. Fakhari, Extended lattice boltzmann scheme for droplet combustion, *Physical Review E* 95 (5) (2017) 053301.

- [15] S. Hosseini, N. Darabiha, D. Thévenin, Mass-conserving advection–diffusion lattice boltzmann model for multi-species reacting flows, *Physica A: Statistical Mechanics and its Applications* 499 (2018) 40–57.
- [16] J. Latt, B. Chopard, Lattice boltzmann method with regularized pre-collision distribution functions, *Mathematics and Computers in Simulation* 72 (2-6) (2006) 165–168.
- [17] O. Malaspinas, B. Chopard, J. Latt, General regularized boundary condition for multi-speed lattice boltzmann models, *Computers & Fluids* 49 (1) (2011) 29–35.
- [18] Y.-L. Feng, S.-L. Guo, W.-Q. Tao, P. Sagaut, Regularized thermal lattice boltzmann method for natural convection with large temperature differences, *International Journal of Heat and Mass Transfer* 125 (2018) 1379–1391.
- [19] R. K. Freitas, A. Henze, M. Meinke, W. Schröder, Analysis of lattice-boltzmann methods for internal flows, *Computers & Fluids* 47 (1) (2011) 115–121.
- [20] M. Gehrke, C. Janßen, T. Rung, Scrutinizing lattice boltzmann methods for direct numerical simulations of turbulent channel flows, *Computers & Fluids* 156 (2017) 247–263.
- [21] I. V. Karlin, F. Bösch, S. Chikatamarla, Gibbs’ principle for the lattice-kinetic theory of fluid dynamics, *Physical Review E* 90 (3) (2014) 031302.

- [22] M. Geier, M. Schönherr, A. Pasquali, M. Krafczyk, The cumulant lattice Boltzmann equation in three dimensions: Theory and validation, *Computers & Mathematics with Applications* 70 (4) (2015) 507–547.
- [23] D. Esch, A. Siripong, R. Pike, Thermodynamic properties in polynomial form for carbon, hydrogen, nitrogen, and oxygen systems from 300 to 15000 k.
- [24] R. J. Kee, F. M. Rupley, J. A. Miller, The chemkin thermodynamic data base, Unknown.
- [25] D. G. Goodwin, H. K. Moffat, R. L. Speth, Cantera: An object-oriented software toolkit for chemical kinetics, thermodynamics, and transport processes, <http://www.cantera.org> (2017).
- [26] P. Boivin, C. Jiménez, A. L. Sánchez, F. A. Williams, An explicit reduced mechanism for H₂–air combustion, *Proceedings of the Combustion Institute* 33 (1) (2011) 517–523.
- [27] F. Williams, et al., Chemical-kinetic mechanisms for combustion applications, University of California, San Diego, <http://web.eng.ucsd.edu/mae/groups/combustion/mechanism.html>.
- [28] T. Schönfeld, M. Rudgyard, Steady and unsteady flows simulations using the hybrid flow solver AVBP, *AIAA Journal* 37 (11) (1999) 1378–1385.
- [29] J. Jacob, O. Malaspinas, P. Sagaut, A new hybrid recursive regularised bhatnagar–gross–krook collision model for lattice boltzmann method-based large eddy simulation, *Journal of Turbulence* (2018) 1–26.

- [30] Y. Feng, P. Boivin, J. Jacob, P. Sagaut, Hybrid recursive regularized lattice boltzmann simulation of humid air with application to meteorological flows, *Physical Review E* 100 (2) (2019) 023304.
- [31] Y. Feng, P. Boivin, J. Jacob, P. Sagaut, Hybrid recursive regularized thermal lattice boltzmann model for high subsonic compressible flows, *Journal of Computational Physics* 394 (2019) 82 – 99.
- [32] L. Merlier, J. Jacob, P. Sagaut, Lattice-boltzmann large-eddy simulation of pollutant dispersion in complex urban environment with dense gas effect: Model evaluation and flow analysis, *Building and Environment* 148 (2019) 634–652.
- [33] J. Jacob, P. Sagaut, Wind comfort assessment by means of large eddy simulation with lattice boltzmann method in full scale city area, *Building and Environment* 139 (2018) 110–124.
- [34] S. Wilhelm, J. Jacob, P. Sagaut, An explicit power-law-based wall model for lattice boltzmann method–reynolds-averaged numerical simulations of the flow around airfoils, *Physics of Fluids* 30 (6) (2018) 065111.
- [35] O. Malaspinas, Increasing stability and accuracy of the lattice boltzmann scheme: recursivity and regularization, arXiv preprint arXiv:1505.06900.
- [36] D. d. Humières, I. Ginzburg, M. Krafczyk, P. Lallemand, L.-S. Luo, Multiple–relaxation–time lattice Boltzmann models in three dimensions, *Phil. Trans. R. Soc. Lond. A* 360 (2002) 437–451.

- [37] F. Dubois, P. Lallemand, Towards higher order lattice Boltzmann schemes, *Journal of Statistical Mechanics: Theory and Experiment* 2009 (06) (2009) P06006.
- [38] K. N. Premnath, J. Abraham, Three-dimensional multi-relaxation time (MRT) lattice-Boltzmann models for multiphase flow, *Journal of Computational Physics* 224 (2) (2007) 539–559.
- [39] H. Xu, O. Malaspinas, P. Sagaut, Sensitivity analysis and determination of free relaxation parameters for the weakly-compressible MRT-LBM schemes, *Journal of Computational Physics* 231 (21) (2012) 7335–7367.
- [40] B. Denet, P. Haldenwang, Numerical study of thermal-diffusive instability of premixed flames, *Combustion science and technology* 86 (1-6) (1992) 199–221.
- [41] B. Denet, P. Haldenwang, A numerical study of premixed flames darrieus-landau instability, *Combustion science and technology* 104 (1-3) (1995) 143–167.
- [42] M. Matalon, Intrinsic flame instabilities in premixed and nonpremixed combustion, *Annu. Rev. Fluid Mech.* 39 (2007) 163–191.
- [43] C. J. Rutland, J. H. Ferziger, Simulations of Flame-Vortex Interactions, *Combustion and Flame* 360 (1991) 343–360.
- [44] S. Kadowaki, T. Hasegawa, Numerical simulation of dynamics of premixed flames: flame instability and vortex-flame interaction, *Progress in energy and combustion science* 31 (3) (2005) 193–241.

- [45] T. Poinso, D. Veynante, S. Candel, Quenching processes and premixed turbulent combustion diagrams, *Journal of Fluid Mechanics* 228 (1991) 561–606.
- [46] W. L. Roberts, J. F. Driscoll, M. C. Drake, L. P. Goss, Images of the quenching of a flame by a vortex—to quantify regimes of turbulent combustion, *Combustion and Flame* 94 (1-2) (1993) 58–69.
- [47] C. Mueller, J. Driscoll, D. Reuss, M. Drake, M. Rosalik, Generation and attenuation of vorticity by flames: measured vorticity field time evolution during a premixed flame–vortex interaction, *Combust Flame* 112 (1998) 342–6.
- [48] P. L. Bhatnagar, E. P. Gross, M. Krook, A model for collision processes in gases. i. small amplitude processes in charged and neutral one-component systems, *Phys. Rev.* 94 (1954) 511–525.
- [49] T. Poinso, D. Veynante, *Theoretical and numerical combustion*, RT Edwards, Inc., 2005.
- [50] K. Kuo, *Principles of combustion*, Wiley New York et al., 1986.
- [51] T. Krüger, H. Kusumaatmaja, A. Kuzmin, O. Shardt, G. Silva, E. M. Viggien, *The Lattice Boltzmann Method: Principles and Practice*, Springer, 2016.
- [52] S. A. Hosseini, N. Darabiha, D. Thévenin, Theoretical and numerical analysis of the lattice kinetic scheme for complex-flow simulations, *Physical Review E* 99 (2) (2019) 023305.

- [53] C. Coreixas, G. Wissocq, G. Puigt, J. F. Boussuge, P. Sagaut, Recursive regularization step for high-order lattice Boltzmann methods, *Physical Review E* 96 (3) (2017) 1–22.
- [54] Y. Feng, P. Sagaut, W. Tao, A three dimensional lattice model for thermal compressible flow on standard lattices, *Journal of Computational Physics* 303 (2015) 514–529.
- [55] S. Gottlieb, C.-W. Shu, E. Tadmor, Strong stability-preserving high-order time discretization methods, *SIAM review* 43 (1) (2001) 89–112.
- [56] E. F. Toro, *Riemann solvers and numerical methods for fluid dynamics: a practical introduction*, Springer Science & Business Media, 2009.
- [57] G. Strang, On the construction and comparison of difference schemes, *SIAM journal on numerical analysis* 5 (3) (1968) 506–517.
- [58] S. Marié, D. Ricot, P. Sagaut, Comparison between lattice boltzmann method and navier–stokes high order schemes for computational aeroacoustics, *Journal of Computational Physics* 228 (4) (2009) 1056–1070.
- [59] D. Fernández-Galisteo, C. Jiménez, M. Sánchez-Sanz, V. N. Kurdyumov, The differential diffusion effect of the intermediate species on the stability of premixed flames propagating in microchannels, *Combustion Theory and Modelling* 18 (4-5) (2014) 582–605.
- [60] P. J. Linstrom, W. Mallard, Nist chemistry webbook; nist standard reference database no. 69.

- [61] M. Baum, Ntmix-ckemkin release 2, user's guide version 1.0, Tech. rep., Technical report, CERFACS, 42, avenue G. Coriolis-31057 Toulouse cedex 1, 1995.
- [62] R. J. Kee, F. M. Rupley, E. Meeks, J. A. Miller, CHEMKIN-III: A FORTRAN chemical kinetics package for the analysis of gas-phase chemical and plasma kinetics, Sandia National Laboratories Livermore, CA, 1996.
- [63] R. Löhner, Towards overcoming the LES crisis, *International Journal of Computational Fluid Dynamics* (2019) 1–11.
- [64] [online] (2018). [link].